J. Plasma Phys. (2019), *vol.* 85, 905850503 © Cambridge University Press 2019
doi:10.1017/S0022377819000588

A comparison of turbulent transport in a quasi-helical and a quasi-axisymmetric stellarator

I. J. McKinney[1],†, M. J. Pueschel[2], B. J. Faber[1], C. C. Hegna[1], J. N. Talmadge[3], D. T. Anderson[3], H. E. Mynick[4] and P. Xanthopoulos[5]

[1]Department of Engineering Physics, University of Wisconsin-Madison, Madison, WI 53706, USA

[2]Institute for Fusion Studies, University of Texas at Austin, Austin, TX 78712, USA

[3]Department of Electrical & Computer Engineering, University of Wisconsin-Madison, Madison, WI 53706, USA

[4]Princeton Plasma Physics Laboratory, Princeton, NJ 08543, USA

[5]Max-Planck-Institut für Plasmaphysik, Wendelsteinstraße 1, 17491 Greifswald, Germany

(Received 27 April 2019; revised 12 August 2019; accepted 13 August 2019)

Ion-temperature-gradient-driven (ITG) turbulence is compared for two quasi-symmetric (QS) stellarator configurations to determine the relationship between linear growth rates and nonlinear heat fluxes. We focus on the quasi-helically symmetric (QHS) stellarator HSX and the quasi-axisymmetric (QAS) stellarator NCSX. In normalized units, HSX exhibits higher growth rates than NCSX, while heat fluxes in gyro-Bohm units are lower in HSX. These results hold for simulations made with both adiabatic and kinetic electrons. The results show that HSX has a larger number of subdominant modes than NCSX and that eigenmodes are more spatially extended in HSX. We conclude that the consideration of nonlinear physics is necessary to accurately assess the heat flux due to ITG turbulence when comparing QS stellarator equilibria.

Key words: fusion plasma, plasma instabilities, plasma nonlinear phenomena

1. Introduction

The stellarator is an appealing fusion reactor concept because plasma discharges are disruption-free in the absence of large plasma currents and steady-state operation is possible (Gates *et al.* 2018). However, the classical stellarator exhibits poor neoclassical transport properties at low collisionality, a by-product of poorly-confined trapped-particle orbits. Neoclassical-transport-optimized stellarator configurations have addressed this issue by forcing the bounce-averaged particle excursion from a flux surface during a banana orbit to near zero (Boozer 1983; Mynick 2006). One specific subset of neoclassical-transport-optimized configurations is that of quasi-symmetric stellarators, including quasi-axisymmetry (e.g. National Compact Stellarator eXperiment (Neilson, Zarnstorff & Lyon 2002)) and quasi-helical symmetry

† Email address for correspondence: imckinney@wisc.edu

(e.g. Helically Symmetric eXperiment (Talmadge *et al.* 2008)), which are the subjects of this work.

HSX has shown that even with the reduction in neoclassical heat transport (Canik *et al.* 2007), there is still an additional component to the experimentally-inferred electron heat transport that is thought to be due to trapped-electron-mode (TEM) turbulence (Guttenfelder *et al.* 2009; Weir 2014; Faber *et al.* 2015). In general, turbulence accesses free energy in thermodynamic forces which subsequently produces turbulent transport fluxes. Turbulence can be driven as a result of drift-wave instabilities such as ion-temperature-gradient driven (ITG) (Rudakov & Sagdeev 1961; Horton, Choi & Tang 1981; Xanthopoulos & Jenko 2007; Mynick, Pomphrey & Xanthopoulos 2010; Xanthopoulos *et al.* 2014) and TEMs (Coppi 1965; Coppi, Rosenbluth & Sagdeev 1967; Kadomtsev & Pogutse 1971; Faber *et al.* 2015). Investigation of ITG turbulence in quasi-symmetric stellarators is the focus of the following set of calculations.

Commonly, linear growth rates γ are used to predict the turbulent transport properties of a given configuration. One example of such an analysis is given by Rewoldt, Ku & Tang (2005), where a comparison of nine different stellarator magnetic geometries is carried out. In this work, linear growth rates as a function of field-line label, ballooning angle, perpendicular wavenumber and η_i, the ratio of the ion-temperature gradient to the ion-density gradient, were systematically examined. One prominent result of these analyses is that HSX exhibits higher growth rates than not only NCSX-BETA (the configuration most similar to the NCSX equilibrium used in the remainder of the present work) but all of the other configurations as well. The direct implication of this result is that one would expect HSX to exhibit larger ITG turbulent transport relative to the other configurations considered. Both verification of Rewoldt's linear results pertaining to the comparison of HSX and NCSX-BETA and the extension of said analysis to nonlinear simulations form the primary focus of this work.

The turbulent transport properties of a given configuration are commonly estimated by employing a quasilinear mixing-length argument. In this method, the nonlinear heat diffusivities χ_i scale as $\sum_{\mathrm{k}_\perp} \gamma/\langle \mathrm{k}_\perp^2 \rangle$ (Jenko, Dannert & Angioni 2005; Pueschel *et al.* 2016), with the field-line average defined as $\langle X \rangle = \int \mathrm{d}\theta X|\Phi|^2 / \int \mathrm{d}\theta |\Phi|^2$, where $\boldsymbol{k}_\perp$ is the perpendicular wavevector of a given mode, Φ is the electrostatic potential and θ labels points along a field line assuming a ballooning-like ansatz for the micro-instability (Dewar & Glasser 1983; Candy, Waltz & Dorland 2004). This approach relies on a simple premise for the saturation of drift-wave turbulence. It is necessary to verify the predictive capabilities of quasilinear proxies against nonlinear simulations, especially over a range of neoclassical-transport-optimized stellarator configurations where the nonlinear saturation physics of the ITG microturbulence may be quite different. Recent semi-analytical work has indicated that there are qualitative differences in the saturation mechanism of ITG turbulence between quasi-helically symmetric and quasi-axisymmetric stellarators (Hegna, Terry & Faber 2018), where the shorter connection lengths present in quasi-helical symmetry allow for lower saturated heat flux levels. Here, we seek to investigate the capability, or lack thereof, of quasilinear theory as a proxy for turbulent transport between two specific quasi-symmetric stellarators.

With this goal in mind, we employ the gyrokinetic turbulence code GENE (Jenko 2000, Gene, see http://www.genecode.org for code details and access), a massively parallel, local and global Vlasov solver, to study ITG turbulence via flux-tube simulations. Computational approaches tend to increase in expense as magnetic

https://doi.org/10.1017/S0022377819000588 Published online by Cambridge University Press

geometries become increasingly non-axisymmetric, and only recently have nonlinear simulations with both kinetic ions and electrons in stellarator geometries been performed (Ishizawa *et al.* 2013, 2014; Faber *et al.* 2015; Helander *et al.* 2015; Proll *et al.* 2015; Ishizawa *et al.* 2017; Nakata, Nunami & Watanabe 2017). In the present work, electrostatic nonlinear gyrokinetic simulations with both adiabatic and kinetic electrons are presented.

The results shown here indicate that both dominant linear growth rates and quasilinear calculations are sometimes inadequate to accurately assess the ITG turbulent transport properties of a given quasi-symmetric stellarator configuration. It should be noted that results presented by Mynick *et al.* (2010) have shown the successful optimization of ITG turbulent transport over a range of quasi-axisymmetric stellarator configurations by using a quasilinear proxy for the nonlinear heat flux. It should also be noted that recent results have successfully reproduced ITG turbulent transport in $|\hat{s}| > 0.5$ helical plasmas using quasilinear estimates that include the effects of zonal flows (Nunami, Watanabe & Sugama 2013; Toda *et al.* 2019). However, as will be discussed here, quasilinear proxies are sometimes problematic for quasi-helically symmetric stellarators, where nonlinear corrections to quasilinear theory play a more important role relative to quasi-axisymmetric configurations.

As measured by normalized linear growth rates $\gamma a/c_s$, where a and c_s are minor radius and ion sound speed, respectively, NCSX has lower growth rates relative to HSX, while HSX has lower electrostatic nonlinear ion heat fluxes Q_i^{es} in gyro-Bohm units, a finding that applies for both adiabatic- and kinetic-electron simulations. In addition to comparing growth rates and heat fluxes, we conduct various analyses of both linear and nonlinear physics and review differences therein between HSX and NCSX.

Two direct implications of this work are that the saturation physics is integral to the turbulent dynamics in quasi-symmetric stellarators and proxies incorporating nonlinear physics must be developed and benchmarked against nonlinear simulations before they can be used to determine turbulent transport trends across quasi-symmetric stellarators. This paper is organized as follows. Section 2 introduces the gyrokinetic framework and the GENE code. In § 3, the concept of quasi-symmetry and the two aforementioned stellarator configurations are discussed. Section 4 presents an analysis of the two configurations in the limit of adiabatic electrons. Section 5 extends the analyses of § 4 by including kinetic electrons. Conclusions are given in § 6.

2. Simulation approach

In this work, the gyrokinetic turbulence code GENE is used to study ITG turbulence via flux-tube simulations of the NCSX and HSX neoclassical-transport-optimized stellarator equilibria outlined in § 3. Relative to fully kinetic simulations, gyrokinetics reduces computational expense by averaging over the gyrophase of the trajectories of charged particles in the presence of a strong magnetic guide field (Brizard & Hahm 2007). GENE solves a system of coupled equations that consists of the Vlasov equation, the Poisson equation and Ampere's law (in simulations with finite β). Further details regarding the equations solved by GENE can be found in Pueschel *et al.* (2011). Using the magnetohydrodynamic (MHD) equilibrium solver VMEC (Hirshman, van Rij & Merkel 1986) to generate the HSX and NCSX geometries, the GIST code (Xanthopoulos *et al.* 2009) then calculates the necessary magnetic geometry data for the desired flux tube at the specified normalized toroidal magnetic flux $s_0 = \Psi/\Psi(a) = (r_{\text{eff}}/a)^2$, where $\Psi(a)$ is the toroidal flux at the plasma boundary and r_{eff} is an effective radial coordinate implicitly defined by the toroidal magnetic flux.

https://doi.org/10.1017/S0022377819000588 Published online by Cambridge University Press

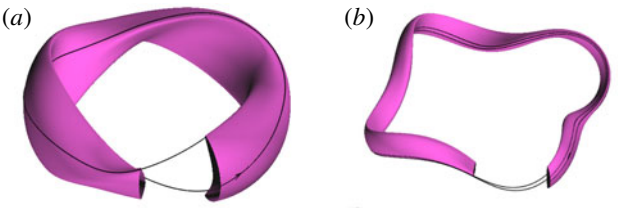

FIGURE 1. The $s_0 \approx 0.5$ flux surfaces of NCSX (a) and HSX (b). The black lines indicate the $\alpha = \theta - \iota\xi = 0$ flux-tube domains of each configuration, where θ and ξ are the poloidal and toroidal angle in Boozer coordinates, respectively.

2.1. *Flux-tube simulation domain*

Due to the computational expense of full-volume and full-flux-surface simulations (Monreal *et al.* 2017), flux-tube simulations are exclusively employed in this work. The characteristic perpendicular length scales of the turbulence in HSX and NCSX are sufficiently small that flux-tube simulations with reduced radial extent will accurately capture the dynamics of the turbulence. In the localized flux-tube simulation domain, periodic and quasi-periodic boundary conditions are used in the radial/binormal and parallel directions, respectively. A flux tube follows a single magnetic field line around the equilibrium with sufficient radial extent to encompass multiple perpendicular turbulent correlation lengths. This requirement prevents artificial self-connection of fluctuations via the periodic radial boundary condition. Care must be taken to ensure that the flux-tube extent along the field line is sufficient so that any given eigenmode is localized and accurately described (Faber *et al.* 2018). In figure 1, examples of $n_{\rm pol} = 2$ flux-tube domains of each configuration are shown, where $n_{\rm pol}$ indicates the number of poloidal transits of the flux tube. The low average magnetic shear in HSX, which affects how extended eigenmodes can be, impacts the convergence characteristics as measured by $n_{\rm pol}$. Prior gyrokinetic studies of HSX flux tubes indicate $n_{\rm pol} = 4$ is required for proper convergence (Faber *et al.* 2018).

In the HSX geometry, the value of the rotational transform $\iota = {\rm d}\Phi_{\rm p}/{\rm d}\Psi = 1/q \approx 1.062$ at $s_0 \approx 0.5$ is near unity, where $\Phi_{\rm p}$ and q are the poloidal magnetic flux and the safety factor, respectively. Contrastingly, NCSX has $\iota \approx 0.559$ at $s_0 = 0.5$. As a result of the near unity value of ι in the HSX geometry, a flux tube in the HSX configuration will require greater $n_{\rm pol}$ to sample more unique portions of the flux surface geometry relative to a flux tube in the NCSX configuration.

3. Quasi-symmetric stellarators

Quasi-symmetry allows for stellarator operation with reduced neoclassical transport due to symmetry in $|\boldsymbol{B}|$, whether that be poloidal, helical or axial symmetry. The magnetic field strength $|\boldsymbol{B}|$ can be written for any stellarator configuration as

$$|\boldsymbol{B}| = B_{00}(\psi)\left[1 + \sum_{m,n} \epsilon_{m,n}(\psi)\cos(n\xi - m\theta)\right], \tag{3.1}$$

where ξ and θ are the toroidal and poloidal angles as written in Boozer coordinates (Boozer 1981, 1983), $B_{00}(\psi)$ is the $(n = 0,\ m = 0)$ component and $\epsilon_{m,n}(\psi)$ denotes the relative strength of the $(n,\ m)$ modes. In quasi-symmetric stellarators, one Fourier

https://doi.org/10.1017/S0022377819000588 Published online by Cambridge University Press

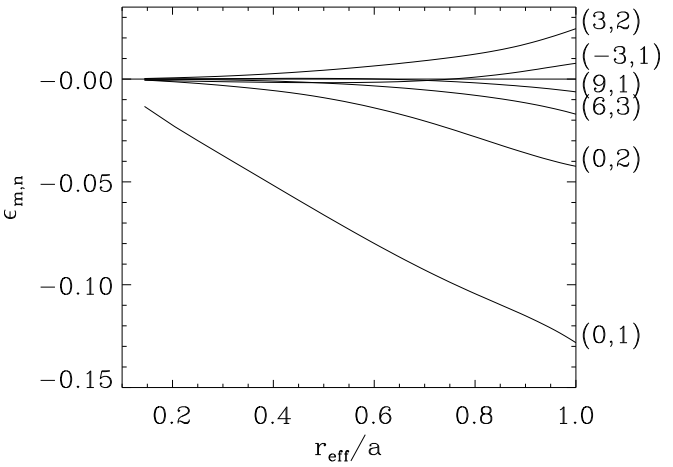

FIGURE 2. The Boozer spectrum for the baseline NCSX equilibrium. Only the six magnetic Fourier modes with the largest amplitude are included. The (0, 0) component is excluded for readability.

mode dominates other components over a majority of the minor radius. In this work, the two quasi-symmetric configurations under consideration are quasi-helical symmetry, specifically the HSX geometry, where the $(n = 4,\ m = 1)$ mode dominates, and quasi-axisymmetry, specifically the NCSX geometry (Mynick *et al.* 2010), where the $(n = 0,\ m = 1)$ mode dominates.

The Boozer spectrum for NCSX given in figure 2 details the relative strength of the six magnetic Fourier modes with the largest amplitude as a function of r_{eff}/a. As shown in figure 2, the (0, 1) mode dominates the magnetic spectrum.

The baseline NCSX equilibrium has total normalized plasma pressure $\beta \approx 4\,\%$, three field periods, aspect ratio $\mathrm{A} \approx 4.5$, mean magnetic field $\langle \mathrm{B} \rangle \approx 1.6\mathrm{T}$ and sizable average magnetic shear $\hat{s} = (r_{\mathrm{eff}}/q)\,\mathrm{d}q/\mathrm{d}r_{\mathrm{eff}} = -(r_{\mathrm{eff}}/\iota)\,\mathrm{d}\iota/\mathrm{d}r_{\mathrm{eff}} \approx -0.5$ at $s_0 \approx 0.5$. It should be noted that average and local magnetic shear are distinct quantities. The average magnetic shear is defined above and is a flux-tube average of the local shear. The local magnetic shear $\hat{s}_{\mathrm{loc}} = (\hat{\boldsymbol{b}} \times \hat{\boldsymbol{n}}) \cdot \boldsymbol{\nabla} \times (\hat{\boldsymbol{b}} \times \hat{\boldsymbol{n}})$ (Greene & Johnson 1968; Hegna 2000), where $\hat{\boldsymbol{b}}$ and $\hat{\boldsymbol{n}}$ are unit vectors in the directions parallel to the magnetic field and locally normal to the flux surface, respectively, can vary significantly with field-line label and along the field line. This distinction will be important later when discussing eigenmode and subdominant mode physics.

HSX enforces helical symmetry by maximizing the magnitude of the (4, 1) component relative to other magnetic modes (Talmadge *et al.* 2008). This can be seen in the HSX Boozer spectrum given in figure 3.

The HSX equilibrium is a four-field-period configuration with aspect ratio $\mathrm{A} \approx 10$, mean magnetic field $\langle \mathrm{B} \rangle \approx 1$ T and low magnetic shear $\hat{s} \approx -0.05$ at $s_0 \approx 0.5$. It should also be noted that HSX is not optimized for a specific normalized plasma pressure β. Thus, the HSX equilibrium used throughout has $\beta = 0\,\%$. The use of the finite-β NCSX equilibrium is motivated by the fact that it is the experimentally-optimized configuration. As such, this bolsters our results, since the NCSX configuration benefits from the β-induced magnetic well in the nonlinear simulations while this effect is not accounted for in the HSX simulations.

https://doi.org/10.1017/S0022377819000588 Published online by Cambridge University Press

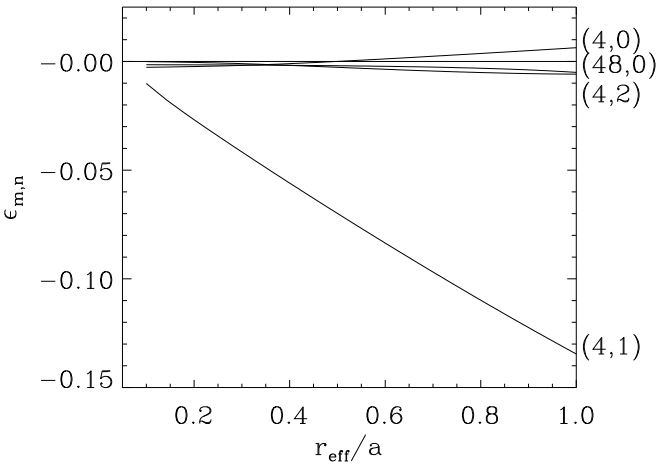

FIGURE 3. The Boozer spectrum for the HSX equilibrium. Only four magnetic Fourier modes are included as subsequent modes lie almost directly on top of either the (4, 2) or (4, 0) mode. The (0, 0) component is omitted for readability.

4. Adiabatic-electron simulations

The first comparison here assumes adiabatic electrons, where electrons have an immediate response to a fluctuating electrostatic potential ($e\Phi/T_{e0} = n_e/n_{e0}$), where e, T_{e0}, n_e, and n_{e0} are the elementary charge, equilibrium electron temperature, fluctuating electron density and equilibrium electron density, respectively. The rationale for this is twofold. First, past work has focused on the adiabatic-electron limit (Rewoldt *et al.* 2005; Mynick *et al.* 2010; Mynick, Pomphrey & Xanthopoulos 2011; Hegna *et al.* 2018) owing in part to the lower computational costs. Second, by first analysing the simpler adiabatic-electron limit, it is possible to see whether trends persist when simulating with kinetic electrons. Results pertaining to linear simulations in the adiabatic-electron limit will be presented next, followed by nonlinear results.

4.1. *Linear eigenmodes*

A normal eigenmode ansatz is applied to the linear equations. Fluctuating quantities are assumed to evolve as Φ, $n \propto \exp[\mathrm{i}(\boldsymbol{k}\cdot\boldsymbol{x} - \omega\mathrm{t})]$. Linear initial-value simulations determine the most unstable eigenmode of the system. Figure 4 shows the dominant growth rate γ at each perpendicular wavenumber $k_\perp\rho_s$, where the most unstable eigenmode is the streamer ($k_x = 0$, $k_\perp = k_y$) and $\rho_s = c_s m_i/(eB)$, where k_x and k_y are the radial and binormal wavenumbers, respectively. In figure 4, the transport-relevant regime is the low-k_y region, as it is the large-wavelength structures that dominate heat and particle flux. The normalized gradient values used for all simulations with adiabatic electrons are $a/L_n = 0$ and $a/L_{Ti} = 3$ where $L_{n,T}^{-1} \equiv -[1/(n_0, T_0)]d(n_0, T_0)/\mathrm{d}r$.

The NCSX configuration exhibits lower growth rates in the low-k_y regime, suggesting that NCSX should display more favourable behaviour with respect to ITG turbulent transport, i.e. a lower electrostatic ion heat flux Q_i^{es} in nonlinear simulations. It should be noted that $a \approx 0.33$ m and $a \approx 0.12$ m for NCSX and HSX, respectively. Therefore, depending on which k_y one considers, there is as much as a factor of 8 difference in unnormalized linear growth rates between HSX and NCSX. This result is consistent with calculations made by Rewoldt *et al.* (2005).

https://doi.org/10.1017/S0022377819000588 Published online by Cambridge University Press

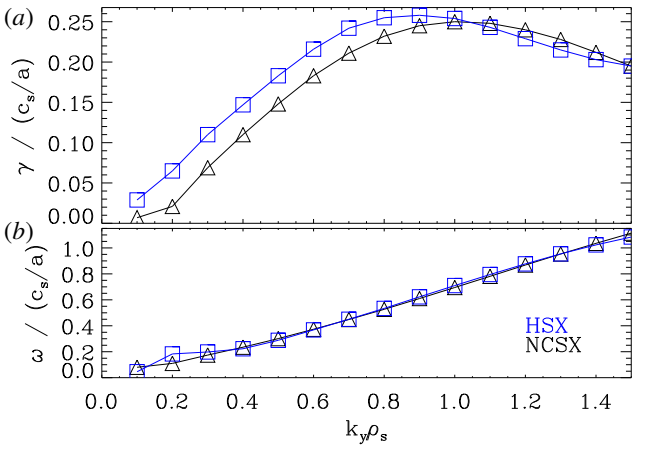

FIGURE 4. The dominant linear growth rate γ (*a*) and real frequency ω (*b*) as a function of normalized binormal wavenumber $k_y\rho_s$ for the NCSX (black triangles) and HSX (blue squares) configurations. These results are from simulations with adiabatic electrons. The dominant mode at each k_y is ITG. NCSX exhibits lower normalized dominant linear growth rates at low k_y compared to HSX.

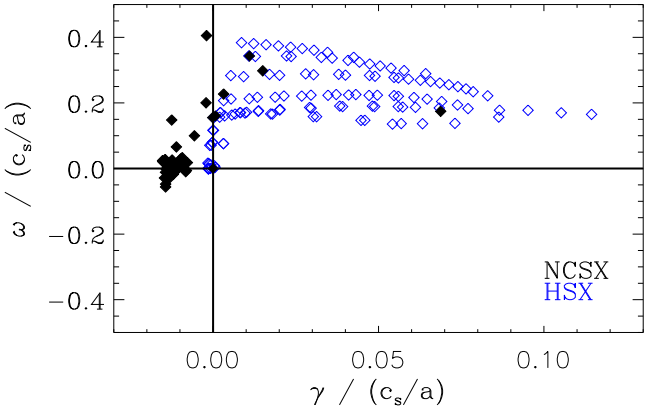

FIGURE 5. The first 123 and 47 linear eigenmodes in HSX (blue hollow diamonds) and NCSX (black filled diamonds), respectively, at binormal wavenumber $k_y\rho_s = 0.3$ for simulations with adiabatic electrons, as determined by GENE's iterative eigenvalue solver.

Next, additional differences in the linear ITG drift-wave physics between NCSX and HSX will be elucidated, including results pertaining to subdominant mode behaviour, eigenmode structure and a quasilinear transport comparison.

4.1.1. *Subdominant mode landscape*

Figure 5 shows a plot of frequency and growth rate of the first 123 and 47 linear eigenmodes for HSX and NCSX, respectively, at $k_y\rho_s = 0.3$. There are 109 and 5 linearly unstable modes in HSX and NCSX, respectively. The larger number of unstable modes in HSX relative to NCSX is characteristic of the subdominant mode landscape at other values of $k_y\rho_s$ in the low-k_y range. Subdominant modes are

https://doi.org/10.1017/S0022377819000588 Published online by Cambridge University Press

eigenmodes of the linear operator of the system that have smaller positive growth rates than the dominant instability.

The motivation for using $k_y\rho_s = 0.3$ for this calculation is that this value of k_y is near the peak of the ion heat flux spectrum in figure 8 for HSX. The large difference between the subdominant eigenmode landscape of HSX and NCSX in this respect is due in large part to the dissimilar average magnetic shear $\hat{s}$ in each configuration. Generally, larger $\hat{s}$ more effectively localizes a given eigenmode to the bad-curvature region. Since $\hat{s}$ is small in HSX, modes are more sensitive to portions of the magnetic geometry further away from the outboard midplane where the local magnetic shear has a small amplitude. With more regions of the magnetic field line available to these eigenmodes due to small $\hat{s}$, HSX exhibits substantially more subdominant modes than NCSX; see also Faber *et al.* (2015) and Pueschel *et al.* (2016). For low magnetic shear, mode localization at different k_x is possible with little penalty, resulting in many concurrently unstable mode branches. One would expect this to bode poorly for turbulent transport in HSX relative to NCSX, especially since there are a number of subdominant modes in HSX that are more unstable than the dominant instability present in NCSX.

It is noteworthy that eigenvalue simulations of HSX with an artificial, NCSX-like $\hat{s} \approx -0.5$ display only a handful of subdominant modes, indicating that $\hat{s}$ does indeed play an important role with respect to the subdominant mode landscape. However, small average shear $\hat{s}$ is not the whole story. The exact structure, especially the peaks and valleys, of the local magnetic shear $\hat{s}_{\rm loc}$ and the curvature $\vec{\kappa} = (\hat{\boldsymbol{b}} \cdot \boldsymbol{\nabla})\hat{\boldsymbol{b}}$ along the field line also play important roles in the dynamics.

The existence of a larger number of unstable modes seems unfavourable with respect to turbulent transport properties; however, this may not necessarily be the case. In a tokamak, the most unstable mode at a given k_y can describe upwards of 70 % of the turbulent state (Pueschel *et al.* 2013), while in a geometry like HSX, all of the unstable modes combined may only constitute 50 % of the nonlinear state (Pueschel *et al.* 2016). This is consistent with the fact that quasilinear proxies can work to predict and optimize ITG turbulent transport over a range of quasi-axisymmetric stellarators, as they are tokamak-like. But, subdominant and stable modes can play a more significant role in a configuration like HSX, providing additional channels for the nonlinear transfer and dissipation of energy.

4.1.2. *Eigenmode structure*

In HSX, eigenmodes at long wavelengths in k_y extend far along the magnetic field line. This differs from the eigenmode structure of NCSX, where eigenmodes are more strongly localized to the bad-curvature region of a given field line, generally at the outboard midplane for quasi-axisymmetric geometries. Figure 6 highlights this trend between NCSX and HSX, showing the electrostatic potential Φ structure of the dominant eigenmode at wavenumber $k_y\rho_s = 0.2$.

The general shape of eigenmodes in a given magnetic geometry is a strong function of the local magnetic shear $\hat{s}_{\rm loc}$ (Faber *et al.* 2018). In general, we observe that eigenmodes tend to avoid regions of large $\hat{s}_{\rm loc}$, consistent with theory (Plunk *et al.* 2014). This disparate eigenmode behaviour can have important implications for the energetics of the turbulent state.

The structure of eigenmodes plays an important role in determining the effectiveness of nonlinear energy transfer from unstable to damped eigenmodes in turbulent saturation physics (Terry, Baver & Gupta 2006; Hatch *et al.* 2009). In a configuration like HSX, where eigenmodes are more extended along the field line, both the

https://doi.org/10.1017/S0022377819000588 Published online by Cambridge University Press

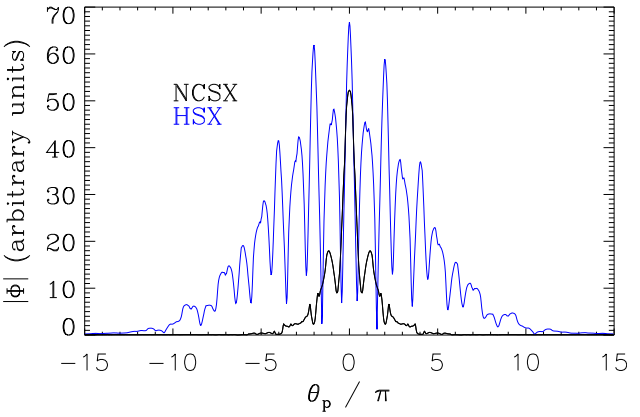

FIGURE 6. Eigenmode amplitude as a function of ballooning angle for binormal wavenumber $k_y\rho_s = 0.2$ for the baseline NCSX configuration (black) and the HSX geometry (blue) for simulations with adiabatic electrons. Note the extended nature of the HSX eigenmode relative to NCSX.

nonlinear coupling between eigenmodes and therefore the nonlinear transfer of energy to stable modes is more efficient (Hegna *et al.* 2018), allowing for lower saturated heat flux levels.

4.1.3. *Quasilinear comparison*

A quasilinear analysis of HSX and NCSX can provide insight into the extent to which the linear physics accurately captures the performance of a given stellarator configuration with respect to ITG turbulence. The goal of this quasilinear analysis is to see if the conclusion of the comparison of dominant linear growth rates between configurations is changed by accounting for all of the subdominant modes at each k_y, the impact of individual mode widths and quasilinear weight changes. To achieve this, one can employ a mixing-length argument to estimate the quasilinear turbulent thermal diffusivity as (Pueschel *et al.* 2016)

$$\chi_i^{QL} = \sum_{k,j} S_k \frac{w_{k,j}\gamma_{k,j}}{\langle k_{\perp k,j}^2 \rangle}, \tag{4.1}$$

where

$$\langle k_\perp^2 \rangle = \langle g^{xx}k_x^2 + 2g^{xy}k_xk_y + g^{yy}k_y^2 \rangle, \tag{4.2}$$

with the field-line average defined as it was in the introduction. The k and j sums are over wavenumbers k_y and the unstable modes, respectively. $\gamma_{k,j}$ is the growth rate of a particular mode and $\langle k_{\perp k,j}^2 \rangle$ is an average square perpendicular wavenumber which accounts for the flux-tube geometry. The shaping factor S_k is determined by the heat flux spectrum of a reference nonlinear simulation. More specifically, S_k relates to the heat flux associated with a specific k_y for a reference nonlinear simulation. For both HSX and NCSX, the reference nonlinear simulations are the simulations from which the time traces in figure 7 are generated. The quasilinear weight $w_{k,j} = Q_i/n^2$, where Q_i and n are the ion heat flux and the fluctuating ion density associated with a specific eigenmode in a linear simulation, is a weighting factor which accounts for the phase information of a given eigenmode, quantifying the extent to which an eigenmode can

https://doi.org/10.1017/S0022377819000588 Published online by Cambridge University Press

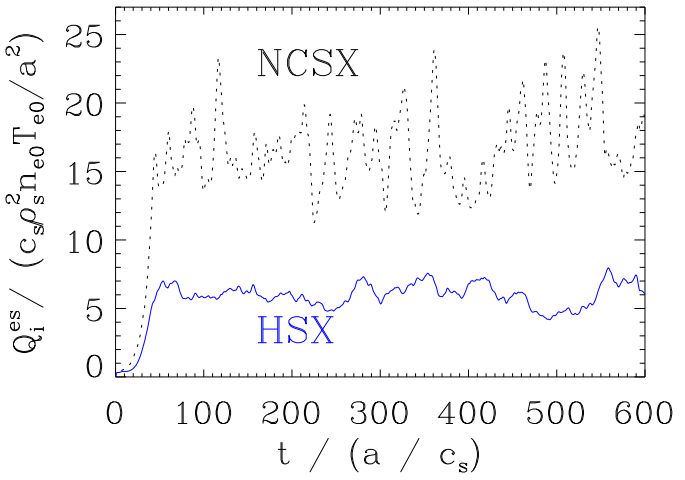

FIGURE 7. Normalized heat flux time traces for HSX (blue solid) and NCSX (black dotted) with adiabatic electrons. The heat flux is approximately 17 and 6 in gyro-Bohm units for NCSX and HSX, respectively, averaged over the quasi-stationary state. The relatively large variation in the NCSX curve relative to HSX is in large part a matter of the radial domain size. Increasing the radial box size would reduce the volume-averaged intermittency of the NCSX heat flux time trace.

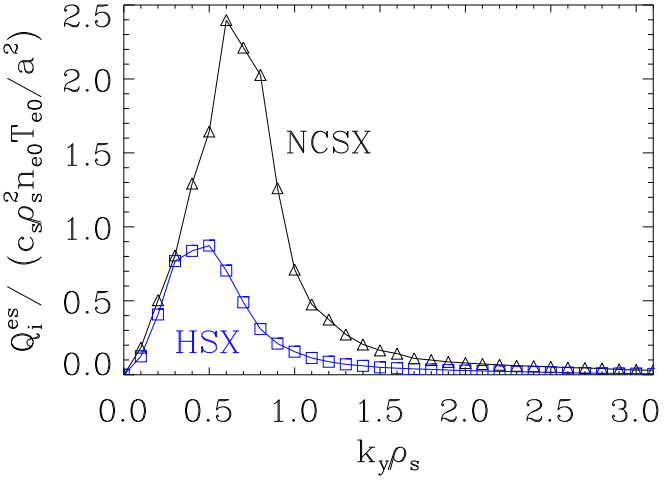

FIGURE 8. The heat flux spectra for HSX (blue squares) and NCSX (black triangles) from nonlinear simulations with adiabatic electrons. Note that the peaks of the nonlinear heat flux spectra of both configurations are to the left of the peaks in linear growth rate for each configuration from figure 4.

contribute to the heat flux. For additional details on the definition of various quantities used in the quasilinear calculation presented here, please see Pueschel *et al.* (2016). In performing this calculation, the subdominant instabilities at each $k_y \rho_s$ are accounted for. Both S_k and $w_{k,j}$ are comparable between the two configurations, with $w_{k,j}$ being approximately 40 % larger on average in HSX. The most notable difference, besides the number of subdominant modes, between HSX and NCSX with respect to this

https://doi.org/10.1017/S0022377819000588 Published online by Cambridge University Press

quasilinear calculation is $\langle k_{\perp k,j}^2 \rangle$, with HSX exhibiting smaller $\langle k_{\perp k,j}^2 \rangle$ than NCSX by roughly an order of magnitude or more, depending on the value of k_y.

A comparison of the quasilinear turbulent thermal diffusivity of HSX and NCSX yields the following result: $(\chi_i^{QL})^{HSX}/(\chi_i^{QL})^{NCSX} \approx 4.2$. This is consistent with an intuitive interpretation of the linear growth rates, as, at low k_y, HSX growth rates are larger than their NCSX counterparts by roughly a factor of 3. Given that this quantity is greater than unity, this shows that HSX performs worse than NCSX linearly even after accounting for all subdominant modes. As shown in the following section, the simple quasilinear estimate is inconsistent with nonlinear simulation results.

4.2. *Nonlinear comparison*

Nonlinear simulations for both HSX and NCSX were performed. Time traces of nonlinear heat flux in gyro-Bohm units for ITG turbulence are presented in figure 7.

The average ion heat flux in gyro-Bohm units is lower in HSX compared to NCSX by nearly a factor of three, a result that is counter-intuitive given that NCSX has lower linear growth rates and associated quasilinear estimates for ITG transport. This indicates both that the ITG turbulence saturation physics is qualitatively different between HSX and NCSX and that standard quasilinear models cannot always be expected to provide good metrics for comparing ITG turbulent transport for these two devices.

With the goal of investigating differences in the ITG turbulence saturation physics between configurations, which could provide insight regarding the mismatch between quasilinear theory and nonlinear gyrokinetic calculations of Q_i^{es}, we examine various aspects of the nonlinear state such as heat flux spectra, cross-phases and nonlinear frequencies in subsequent sections.

4.2.1. *Flux spectra*

Nonlinear heat flux spectra illustrate which values of k_y dominate the heat transport in the quasi-stationary state. Figure 8 shows the heat flux spectra for both NCSX and HSX.

The HSX heat flux spectrum peaks at slightly smaller k_y than the NCSX heat flux spectrum, indicating that larger-wavelength fluctuations are responsible for a greater fraction of the turbulent heat transport in HSX relative to NCSX, where somewhat smaller structures dominate the transport. Both spectra exhibit peaks that are below the peak in linear growth rate γ observed in figure 4, a nonlinear downshift that is consistent with behaviour seen in tokamak simulations (Citrin *et al.* 2017).

4.2.2. *Cross-phases*

We investigate the nonlinear cross-phase α between the electrostatic potential Φ and the total perturbed ion temperature $T_i^{tot} = (2T_{i\perp} + T_{i\parallel})/3$. The relative phase of these two quantities affects the efficiency of the ITG drive as well as that of the $E \times B$ flux. Maximal outward energy transport occurs when the cross-phase between Φ and T_i^{tot} is close to $\pi/2$ and becomes less efficient as the phase difference approaches 0 or π. Negative cross-phases are associated with inward transport and the stable branch of the linear ITG mode. The colour in figure 9 denotes a probability distribution function at each k_y separately, which provides information on how likely it is that any given mode in the nonlinear system exhibits a cross-phase that lies in a small interval about some α. Figure 9 shows the cross-phases for both HSX and NCSX.

https://doi.org/10.1017/S0022377819000588 Published online by Cambridge University Press

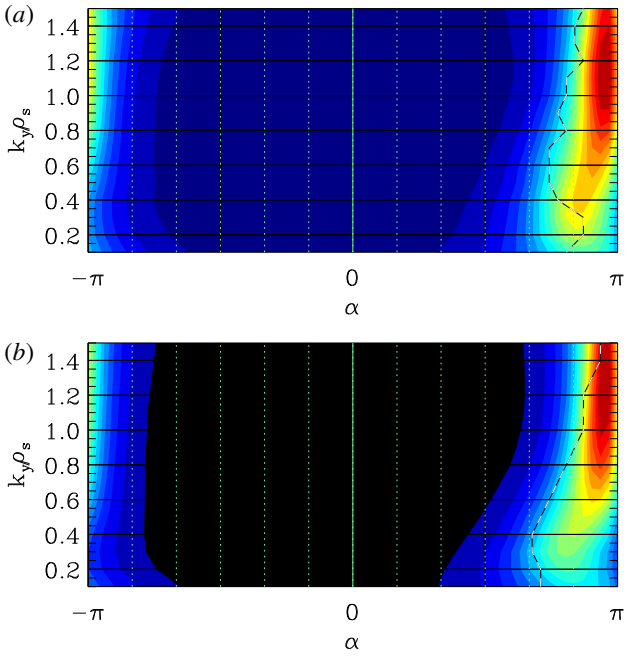

FIGURE 9. The probability distribution function for the nonlinear cross-phase α between Φ and T_i^{tot} for the NCSX (*a*) and HSX (*b*) configurations from simulations with adiabatic electrons. Cross-phases of the dominant linear eigenmode (black dashed curve) are included for comparison. The colour scale for the nonlinear cross-phases is linear. Red indicates regions where there is a higher likelihood that a given mode will exhibit a particular value of the cross-phase.

Clearly, both configurations exhibit very similar phase characteristics, both in terms of the dominant linear eigenmode and the turbulence. A moderate difference is observed in the nonlinear data at $k_y\rho_s < 0.6$, where the phase is less peaked for the HSX configuration, which may be interpreted as a consequence of the more complex subdominant eigenmode landscape. This interpretation is consistent with the fact that at higher $k_y\rho_s$, the number of subdominant modes decreases significantly in the HSX geometry. For example, at $k_y\rho_s = 1.5$, there are only 16 subdominant modes for HSX as opposed to the 108 subdominant modes at $k_y\rho_s = 0.3$. We also note that the difference between the nonlinear data and the dominant linear eigenmode is larger in HSX relative to NCSX at $k_y\rho_s < 0.6$. We deduce this by observing from the cross-phase plots that at $k_y\rho_s < 0.6$, in HSX, the linear cross-phase extends further toward $\pi/2$, whereas in NCSX, the linear cross-phase is much closer to π at low k_y. It is important to highlight that this linear–nonlinear-cross-phase difference applies to the dominant mode in each configuration, and an analysis that includes more subdominant modes may draw other conclusions. Overall, there is a moderate difference in cross-phases between HSX and NCSX, but the difference is not significant enough to merit a phase-based explanation for the mismatch between growth rates and heat fluxes.

4.2.3. *Nonlinear frequency spectra*

The nonlinear frequency spectrum describes the extent to which a fluctuation with a given frequency is present in the nonlinear state as a function of k_y (Faber *et al.* 2015; Pueschel *et al.* 2016). Figure 10 depicts the nonlinear frequencies as a function

https://doi.org/10.1017/S0022377819000588 Published online by Cambridge University Press

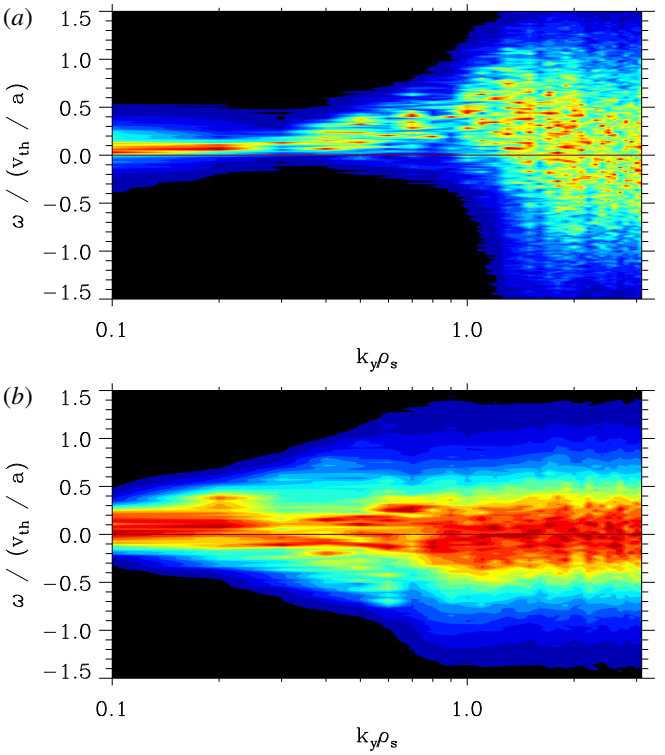

FIGURE 10. The nonlinear frequency spectra for the NCSX (*a*) and HSX (*b*) configurations from simulations with adiabatic electrons. The colour scale has arbitrary units and is linear and normalized at each k_y separately. The broadband features in the HSX spectrum relative to the peaked NCSX spectrum indicate that the turbulence is comprised of a larger number of excited linear eigenmodes in HSX.

of k_y, highlighting the impact of the subdominant mode landscape on the nonlinear system.

Here, we see a stark difference between the two configurations. In NCSX, the frequency spectrum is very peaked, especially in the low-k_y range, where the system is dominated by only a narrow band of frequencies. Contrastingly, HSX exhibits a more broadband frequency structure at all values of k_y, suggesting that no single mode is dominating the system, and that the nonlinear state is comprised of a large number of modes. Note that while NCSX also has a broadband frequency spectrum at high k_y, this is less relevant to the transport dynamics which is dominated by low-k_y.

The dissimilarities between the nonlinear frequency spectra of HSX and NCSX put forward an explanation for the mismatch between quasilinear predictions and Q_i^{es}. Additional subdominant modes and more extended eigenmode structures present in HSX allow for additional and more efficient channels of nonlinear energy transfer to stable modes, where energy can be dissipated. It has been shown by Hegna *et al.* (2018), where a fluid model is used to identify efficient energy transfer channels to stable modes via three-wave interaction, that energy transfer to stable modes via nonlinear three-wave coupling is more efficient in HSX relative to NCSX. This is in large part due to the extended nature of linear eigenmodes as well as the shorter

https://doi.org/10.1017/S0022377819000588 Published online by Cambridge University Press

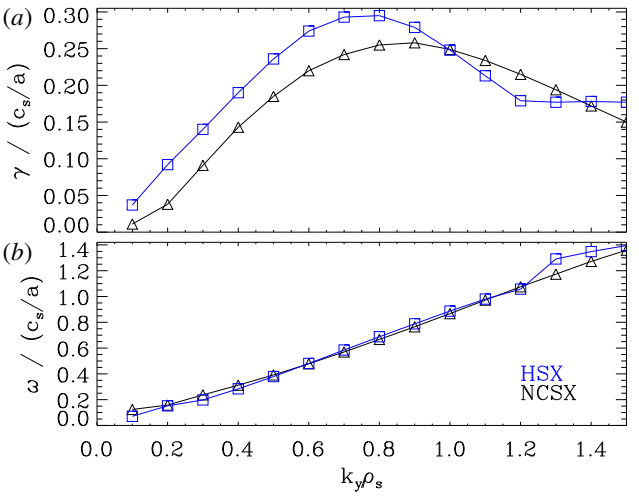

FIGURE 11. Linear growth rate γ (a) and real frequency ω (b) as a function of normalized binormal wavenumber $k_y\rho_s$ for HSX (blue squares) and NCSX (black triangles) from simulations with kinetic electrons. Note that the real frequencies for the kinetic-electron case are almost identical to the adiabatic-electron results.

connection lengths in HSX, which allow for more enhanced resonance and interaction of modes in the nonlinear state. The ITG saturation mechanism can take advantage of additional extended subdominant modes, yielding a lower saturated heat flux level in HSX.

5. Kinetic-electron simulations

Electron physics such as trapping and parallel streaming are included in simulations with kinetic electrons. This can modify the adiabatic-electron results as additional modes such as TEM or electron-temperature gradient (ETG) can impact the dynamics. For the remainder of this work, reference to 'kinetic electrons' will also imply that the normalized plasma pressure β is equal to 0.05 % in the GENE simulations (Pueschel, Kammerer & Jenko 2008). In this limit, the transport is dominantly electrostatic. Fully electromagnetic nonlinear simulations at more appreciable β are deferred for future work, as an ongoing study indicates that the strong ion-temperature gradients used here severely lower the threshold for kinetic ballooning modes.

5.1. *Linear eigenmodes*

In figure 11, the linear growth rate spectrum is plotted for HSX and NCSX using kinetic electrons. Note the trend observed in the adiabatic-electron simulations is still present in the kinetic-electron calculation: NCSX exhibits lower growth rates in the transport-relevant low-k_y regime. Normalized gradient and temperature ratio values used throughout the kinetic-electron simulations presented here are as follows: $a/L_n = a/L_{Te} = T_e/T_i = 1$ and $a/L_{Ti} = 3$.

The large number of subdominant modes present and the characteristic extended eigenmode structures in HSX relative to NCSX discussed in § 4.1 in the adiabatic-electron limit are qualitatively the same when kinetic electrons are included in the simulation. For example, at $s_0 \approx 0.5$ and $k_y\rho_s = 0.2$, NCSX exhibits only one

https://doi.org/10.1017/S0022377819000588 Published online by Cambridge University Press

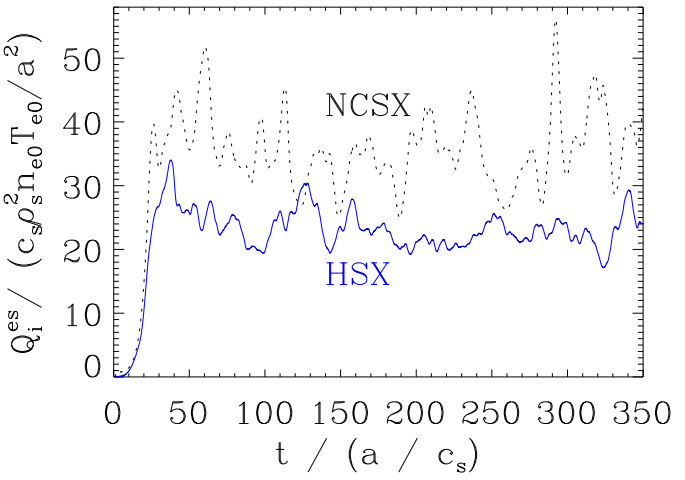

FIGURE 12. Heat flux time traces for the HSX (blue solid line) and NCSX (black dashed line) configurations from simulations with kinetic electrons. The average heat flux in each configuration is approximately 36 and 23 for NCSX and HSX, respectively, again averaged over the quasi-stationary state. We note that the heat flux for HSX (NCSX) increases by approximately a factor of 4 (2) comparing from adiabatic- to kinetic-electron simulations. However, the average heat flux is still lower in HSX relative to NCSX.

subdominant mode in the kinetic-electron regime versus the few subdominant modes present in simulations with adiabatic electrons. Similarly, for NCSX, eigenmodes continue to be localized and centred at the outboard midplane in the bad-curvature region; likewise, for the HSX geometry, eigenmodes are more extended along the field line, especially at low k_y, and the subdominant mode landscape of HSX with kinetic electrons is comprised of an order of magnitude or more subdominant modes compared to NCSX.

5.2. *Nonlinear comparison*

Heat flux time traces for NCSX and HSX are shown in figure 12 for simulations with kinetic electrons. The nonlinear heat flux in gyro-Bohm units is higher for NCSX relative to HSX. This result is consistent with the adiabatic-electron simulations. However, the difference is less than a factor of 1.6 here compared to the factor of approximately 3 observed in adiabatic-electron simulations.

Next, we turn our attention toward the heat flux spectra, the Φ and T_i^{tot} cross-phases, and the nonlinear frequency spectra from simulations with kinetic electrons. The heat flux spectra from nonlinear simulations with kinetic electrons shown in figure 13 indicate that the general shape and peak of both the HSX and NCSX spectra are comparable to the analogous adiabatic-electron result shown in figure 8.

The peak of the HSX heat flux spectra is still at lower k_y than the NCSX peak, indicating that larger-wavelength structures still dominate the heat flux in HSX relative to NCSX. It is worth noting that the peak in the Q_i^{es} flux spectra of each configuration shifts to larger scales relative to their adiabatic-electron analogues. This shift is consistent with the shift in the peak linear growth rate γ when going from adiabatic- to kinetic-electron simulations.

Relative to the adiabatic-electron results (figure 9), the nonlinear cross-phases between Φ and T_i^{tot} for HSX and NCSX from kinetic-electron simulations (figure 14)

https://doi.org/10.1017/S0022377819000588 Published online by Cambridge University Press

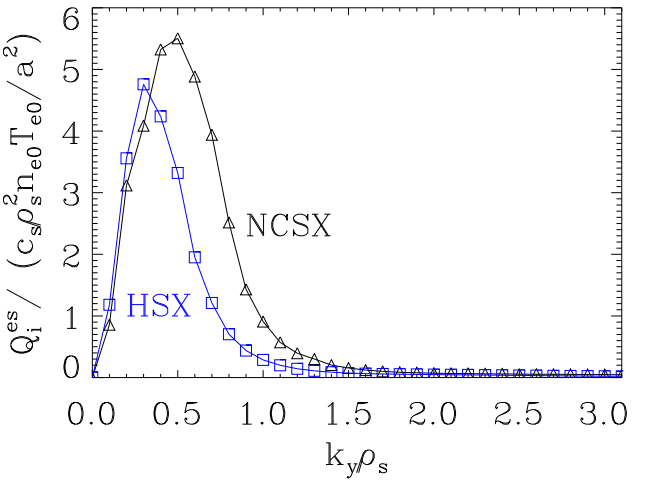

FIGURE 13. Heat flux spectra for HSX (blue squares) and NCSX (black triangles) with kinetic electrons. The flux spectrum peak is at lower k_y for HSX versus NCSX. The peaks of both spectra are at lower k_y relative to their adiabatic-electron analogues.

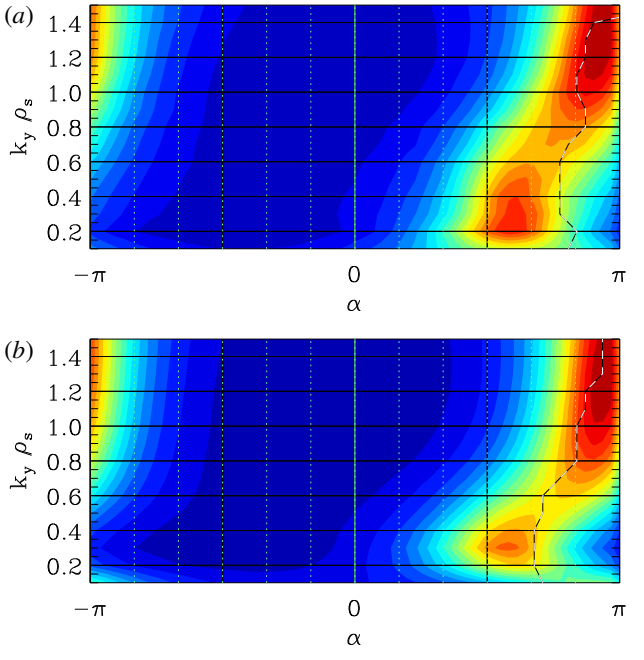

FIGURE 14. The probability distribution function for the nonlinear cross-phase between Φ and T_i^{tot} for simulations of NCSX (*a*) and HSX (*b*) with kinetic electrons. Linear cross-phases of the dominant linear eigenmode are overlaid (black dashed curve) for comparison. The nonlinear cross-phase colour scale is linear. Qualitatively, these cross-phases are similar to their adiabatic-electron analogues with the exception of the low-k_y blob at $\pi/2$ in each configuration.

exhibit an additional low-k_y feature that extends much closer to $\pi/2$, suggesting that drive physics as well as transport are more efficient. This is consistent with the fact that the heat fluxes of both HSX and NCSX are higher in simulations with kinetic

https://doi.org/10.1017/S0022377819000588 Published online by Cambridge University Press

electrons. Cross-phases between Φ and $T_{\mathrm{i}}^{\mathrm{tot}}$ from simulations with kinetic electrons are presented in figure 14.

Similar to the adiabatic-electron case, the nonlinear cross-phases are very similar for both configurations. One observes a moderate mismatch between the linear and nonlinear phases for each configuration at low k_y, a region with a slightly stronger phase signature for HSX, potentially a result of the transport peaking at lower k_y in that configuration.

Lastly, we look at nonlinear frequency spectra in simulations with kinetic electrons. As was the case in the adiabatic-electron simulations, the nonlinear frequency spectra in the kinetic-electron case suggests that the difference in linear subdominant mode physics between configurations has an impact on the quasi-stationary state of the turbulence. While the difference between the nonlinear frequency spectra of each configuration is less stark in kinetic-electron simulations, there is still a distinct difference in the $0.2 < k_y\rho_{\mathrm{s}} < 0.6$ range where the frequency spectrum of HSX is distinctly broadband relative to NCSX, where it is very much peaked over that same range. This is especially important since it is these length scales that dominate the transport. While the difference in nonlinear frequency spectra is especially clear for the adiabatic-electron clear ITG regime, we expect it to be more complex for significantly stronger a/L_{n} or $a/L_{T\mathrm{e}}$, as TEMs and potentially KBMs will complicate the subdominant mode landscape. At low k_y, for HSX, figure 15 would suggest that there are a large number of modes contributing to the nonlinear state compared to relatively few modes for NCSX. It is also worth noting that there are qualitative differences at high-k_y between the nonlinear frequency spectra from adiabatic-electron (figure 10) and kinetic-electron (figure 15) simulations for both configurations. However, given that the dynamics of ITG turbulence is dominated by low-k_y behaviour, it is unlikely that these qualitative differences play a significant role in setting transport levels.

In summary, the transition from adiabatic- to kinetic-electron simulations produces relatively little in terms of qualitative changes to the linear and nonlinear physics in both configurations, aside from the low-k_y feature in the nonlinear cross-phases, which is consistent with the increased transport values in the kinetic-electron nonlinear simulations.

6. Conclusions

Results presented here include both linear and nonlinear gyrokinetic simulations of ITG turbulence for two specific quasi-symmetric stellarator configurations, HSX (quasi-helical symmetry) and NCSX (quasi-axial symmetry). Simulations with both adiabatic and kinetic electrons are performed. Linear eigenvalue simulations show that HSX exhibits a large number of subdominant ITG modes whereas only a few subdominant modes are present in NCSX. Eigenmodes are much more extended along the field line in HSX, due to the small average magnetic shear at $s_0 \approx 0.5$. In contrast, NCSX has localized eigenmodes centred in the bad curvature region at the outboard midplane. The most unstable ITG mode has a smaller normalized growth rate in NCSX compared to HSX, especially in the transport-relevant low-k_y regime. This is consistent with the results of previous work comparing HSX and NCSX by Rewoldt *et al.* (2005). However, nonlinear simulations reveal that, contrary to expectations based on either linear or quasilinear calculations, HSX has significantly lower heat fluxes in gyro-Bohm units compared to NCSX, especially in the limit of adiabatic electrons. Further investigations into instabilities and turbulence at finite β, as well as into saturation mechanisms, are also underway as future work.

https://doi.org/10.1017/S0022377819000588 Published online by Cambridge University Press

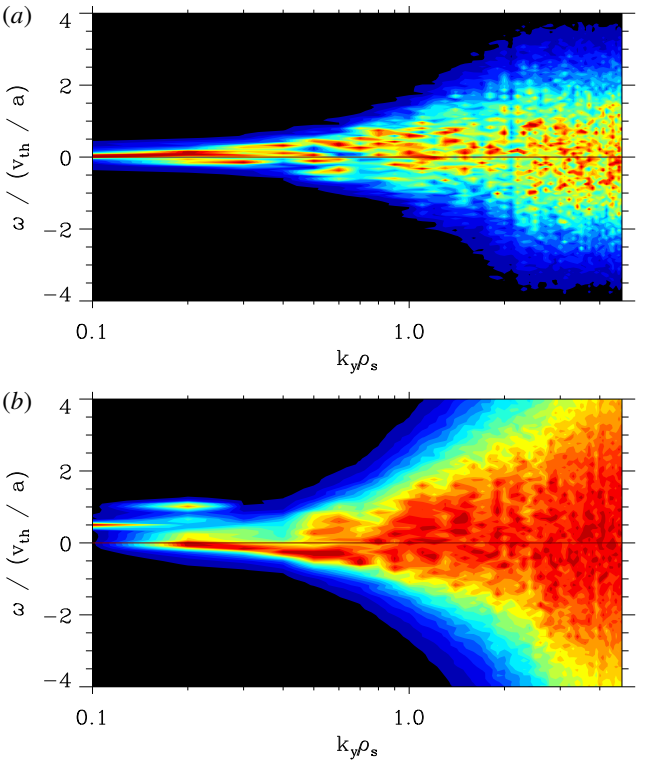

FIGURE 15. Nonlinear frequency spectra of NCSX (*a*) and HSX (*b*) from simulations with kinetic electrons indicate that qualitative trends between the two configurations persist when going from adiabatic- to kinetic-electron simulations. The colour scale is linear and normalized at each $k_y\rho_s$ separately and its units are arbitrary.

Arguably, comparing nonlinear heat fluxes in gyro-Bohm units may not be the most appropriate metric to use when comparing two magnetic geometries of differing aspect ratio. As noted by Helander *et al.* (2015), the total power crossing a flux surface $P = \int \boldsymbol{Q} \cdot \mathrm{d}\boldsymbol{S}$ is potentially a more appropriate quantity for such a comparison between HSX and NCSX. To lowest order, assuming that the plasma parameters are the same between configurations, this quantity P is equal to the gyro-Bohm-normalized heat flux multiplied by a geometric factor that is approximately the aspect ratio. Since the aspect ratio of HSX is approximately two times as large as the aspect ratio of NCSX, a factor of two increase in the HSX heat flux would be needed for a proper comparison of HSX and NCSX, given the normalization. While this conversion factor changes the quantitative measures of the turbulent transport, this does not change the conclusions of this work, as linear calculations would lead one to expect that HSX should perform worse than NCSX with respect to ITG turbulent transport by up to as much as a factor of 8, depending on growth rate normalization. Using peak linear growth rates as a measure for turbulent transport is not a reliable indicator for quasi-symmetric stellarators.

As outlined in this work, differences in the subdominant mode landscape and characteristic eigenmode structure, which are not captured by dominant linear growth rates, can impact the nonlinear ITG turbulence saturation dynamics. Thus, proxies based on nonlinear physics for quantities such as ITG turbulent transport must be

https://doi.org/10.1017/S0022377819000588 Published online by Cambridge University Press

developed and properly compared against nonlinear simulations before they can be used to predict Q_i^{es} across quasi-symmetric stellarator designs.

We see, especially through nonlinear frequency spectra, that the ITG turbulence is qualitatively different between HSX and NCSX. The turbulent state is comprised of a large number of concurrently excited modes in HSX versus NCSX where only a few modes dominate the system, especially at low k_y. A potential explanation for how this qualitative difference could lead to lower saturated heat flux is as follows.

A theory for ITG turbulent saturation in stellarators has recently been developed that suggests that quasi-helically symmetric stellarators have an intrinsic advantage with regard to turbulent saturation physics relative to other configurations (Hegna *et al.* 2018). The theory relies on a paradigm of nonlinear energy transfer from unstable to damped eigenmodes at comparable wavelength as the dominant saturation process (Terry *et al.* 2018). This process is enabled by a three-wave interaction where the third mode, either a zonal or marginally stable mode, depending upon the properties of the magnetic geometry, primarily regulates the nonlinear energy transfer rate. Quantification of the metrics emerging from the theory suggests that quasi-helical symmetry has much larger nonlinear energy transfer rates relative to quasi-axial symmetry, suggesting lower turbulence levels and reduced turbulent transport. This difference is primarily due to the relatively short connection lengths present in quasi-helical symmetry, which enable strong three-wave interaction between turbulent eigenmodes of the system. More extended eigenmodes in HSX facilitate better nonlinear coupling between modes, producing more efficient transfer of energy to stable modes. The calculations presented here are consistent with the above explanation for the evolution of the energetics of the ITG turbulence, providing an explanation for why HSX saturates at a lower heat flux level than NCSX in nonlinear simulations.

Acknowledgements

The authors acknowledge useful conversations with P. Terry. This material is based on the work supported by the US Department of Energy, Office of Science, Fusion Energy Sciences, under awards no. DE-FG02-93ER54222, no. DE-FG02-04ER54742 and no. DE-FG02-99ER54546. Computing time was provided through the National Energy Research Scientific Computing Center, a DOE Office of Science User Facility, grant no. DE-AC02-05CH11231.

Appendix. Simulation parameters

GENE simulates a five-dimensional phase space where the coordinate system is comprised of the x (radial, Fourier space), y (binormal, Fourier space), z (parallel to the magnetic field), v (parallel velocity space) and w (perpendicular velocity space) directions. For each direction, there is an associated box size l and resolution n. Typical box sizes, resolutions, $k_y^{\min}$ (the smallest binormal wavenumber of the simulation), and hyperdiffusion coefficients (Pueschel, Dannert & Jenko 2010) for HSX (NCSX) are as follows: $n_x = 128$ (128), $n_y = 48$ (48), $n_z = 512$ (128), $k_y^{\min} = 0.1$ (0.1), $l_x = 109\rho_s$ ($182\rho_s$), $n_w = 8$ (8), $n_v = 48$ (48), $n_{\text{pol}} = 4$ (1), $D_z = 8$ (8) and $D_v = 2$ (2).

REFERENCES

BOOZER, A. H. 1981 Plasma equilibrium with rotational magnetic surfaces. *Phys. Fluids* **24** (11), 1999.

BOOZER, A. H. 1983 Transport and isomorphic equilibria. *Phys. Fluids* **26** (2), 496–499.

https://doi.org/10.1017/S0022377819000588 Published online by Cambridge University Press

BRIZARD, A. J. & HAHM, T. S. 2007 Foundations of nonlinear gyrokinetic theory. *Rev. Mod. Phys.* **79** (2), 421–468.

CANDY, J., WALTZ, R. E. & DORLAND, W. 2004 The local limit of global gyrokinetic simulations. *Phys. Plasmas* **11** (5), L25–L28.

CANIK, J. M., ANDERSON, D. T., ANDERSON, F. S. B., CLARK, C., LIKIN, K. M., TALMADGE, J. N. & ZHAI, K. 2007 Reduced particle and heat transport with quasisymmetry in the helically symmetric experiment. *Phys. Plasmas* **14** (5), 056107.

CITRIN, J., ARNICHAND, H., BERNARDO, J., BOURDELLE, C., GARBET, X., JENKO, F., HACQUIN, S., PUESCHEL, M. J. & SABOT, R. 2017 Comparison between measured and predicted turbulence frequency spectra in ITG and TEM regimes. *Phys. Plasmas* **59** (6), 064010.

COPPI, B. 1965 'Universal' instabilities from plasma moment equations. *Phys. Lett.* **14** (3), 172–174.

COPPI, B., ROSENBLUTH, M. N. & SAGDEEV, R. Z. 1967 Instabilities due to temperature gradients in complex magnetic field configurations. *Phys. Fluids* **10** (3), 582.

DEWAR, R. L. & GLASSER, A. H. 1983 Ballooning mode spectrum in general toroidal systems. *Phys. Fluids* **26** (10), 3038–3052.

FABER, B. J., PUESCHEL, M. J., PROLL, J. H. E., XANTHOPOULOS, P., TERRY, P. W., HEGNA, C. C., WEIR, G. M., LIKIN, K. M. & TALMADGE, J. N. 2015 Gyrokinetic studies of trapped electron mode turbulence in the Helically Symmetric eXperiment stellarator. *Phys. Plasmas* **22** (7), 072305.

FABER, B. J., PUESCHEL, M. J., TERRY, P. W., HEGNA, C. C. & ROMAN, J. E. 2018 Stellarator microinstabilities and turbulence at low magnetic shear. *J. Plasma Phys.* **84** (5), 905840503.

GATES, D. A., ANDERSON, D. T., ANDERSON, F. S. B., ZARNSTORFF, M., SPONG, D. A., WEITZNER, H., NEILSON, G. H., RUZIC, D. N., ANDRUCZYK, D., HARRIS, J. H. *et al.* 2018 Stellarator research opportunities: a report of the National Stellarator Coordinating Committee. *J. Fusion Energy* **37** (1), 51–94.

GREENE, J. M. & JOHNSON, J. L. 1968 Interchange instabilities in ideal hydromagnetic theory. *Plasma Phys.* **10**, 729–745.

GUTTENFELDER, W., ANDERSON, D. T., ANDERSON, F. S. B., CANIK, J. M., LIKIN, K. M. & TALMADGE, J. N. 2009 Edge turbulence measurements in electron-heated Helically Symmetric Experiment plasmas. *Phys. Plasmas* **16** (8), 082508.

HATCH, D. R., TERRY, P. W., NEVINS, W. M. & DORLAND, W. 2009 Role of stable eigenmodes in gyrokinetic models of ion temperature gradient turbulence. *Phys. Plasmas* **16** (2), 022311.

HEGNA, C. C. 2000 Local three-dimensional magnetostatic equilibria. *Phys. Plasmas* **7** (10), 3921.

HEGNA, C. C., TERRY, P. W. & FABER, B. J. 2018 Theory of ITG turbulent saturation in stellarators: identifying mechanisms to reduce turbulent transport. *Phys. Plasmas* **25** (2), 022511.

HELANDER, P., BIRD, T., JENKO, F., KLEIBER, R., PLUNK, G. G., PROLL, J. H. E., RIEMANN, J. & XANTHOPOULOS, P. 2015 Advance in stellarator gyrokinetics. *Nucl. Fusion* **55** (5), 053030.

HIRSHMAN, S. P., VAN RIJ, W. I. & MERKEL, P. 1986 Three-dimensional free boundary calculations using a spectral Green's function method. *Comput. Phys. Commun.* **43** (1), 143–155.

HORTON, W. JR, CHOI, D.-I. & TANG, W. M. 1981 Toroidal drift modes driven by ion pressure gradients. *Phys. Fluids* **24** (6), 1077.

ISHIZAWA, A., KISHIMOTO, Y., WATANABE, T.-H., SUGAMA, H., TANAKA, K., SATAKE, S., KOBAYASHI, S., NAGASAKI, K. & NAKAMURA, Y. 2017 Multi-machine analysis of turbulent transport in helical systems via gyrokinetic simulation. *Nucl. Fusion* **57** (6), 066010.

ISHIZAWA, A., MAEYAMA, S., WATANABE, T.-H., SUGAMA, H. & NAKAJIMA, N. 2013 Gyrokinetic turbulence simulations of high-beta taokamak and helical plasmas with full-kinetic and hybrid models. *Nucl. Fusion* **53** (5), 053007.

ISHIZAWA, A., WATANABE, T.-H., SUGAMA, H., MAEYAMA, S. & NAKAJIMA, N. 2014 Electromagnetic gyrokinetic turbulence in finite-beta helical plasmas. *Phys. Plasmas* **21** (5), 055905.

JENKO, F. 2000 Massively parallel Vlasov simulation of electromagnetic drift-wave turbulence. *Compur. Phys. Commun.* **125**, 196–209.

https://doi.org/10.1017/S0022377819000588 Published online by Cambridge University Press

JENKO, F., DANNERT, T. & ANGIONI, C. 2005 Heat and particle transport in a tokamak: advances in nonlinear gyrokinetics. *Plasma Phys. Control. Fusion* **47** (12B), B195–B206.

KADOMTSEV, B. B. & POGUTSE, O. P. 1971 Trapped particles in toroidal magnetic systems. *Nucl. Fusion* **11**, 67–92.

MONREAL, P., SÁNCHEZ, E., CALVO, I., BUSTOS, A., PARRA, F. I., MISHCHENKO, A., KÖNIES, A. & KLEIBER, R. 2017 Semianalytical calculation of the zonal-flow oscillation frequency in stellarators. *Plasma Phys. Control. Fusion* **59** (6), 065005.

MYNICK, H. E. 2006 Transport optimization in stellarators. *Phys. Plasmas* **13** (5), 058102.

MYNICK, H. E., POMPHREY, N. & XANTHOPOULOS, P. 2010 Optimizing stellarators for turbulent transport. *Phys. Rev. Lett.* **105** (9), 095004.

MYNICK, H. E., POMPHREY, N. & XANTHOPOULOS, P. 2011 Reducing turbulent transport in toroidal configurations via shaping. *Phys. Plasmas* **18**, 056101.

NAKATA, M., NUNAMI, M. & WATANABE, T.-H. 2017 Isotope effects on trapped-electron-mode driven turbulence and zonal flows in helical and tokamak plasmas. *Phys. Rev. Lett.* **118** (16), 165002.

NEILSON, G. H., ZARNSTORFF, M. C., LYON, J. F. & THE NCSX TEAM 2002 Quasi-symmetry in stellarator research 5. Status of physics design of quasi-axisymmetry stellarators 5.1 Physics design of the National Compact Stellarator Experiment. *J. Plasma Fusion Res.* **78** (3), 214–219.

NUNAMI, M., WATANABE, T.-H. & SUGAMA, H. 2013 A reduced model for ion temperature gradient turbulent transport in helical plasmas. *Phys. Plasmas* **20** (9), 092307.

PLUNK, G. G., HELANDER, P., XANTHOPOULOS, P. & CONNOR, J. W. 2014 Collisionless microinstabilities in stellarators. III. The ion-temperature-gradient mode. *Phys. Plasmas* **21** (3), 032112.

PROLL, J. H. E., MYNICK, H. E., XANTHOPOULOS, P., LAZERSON, S. A. & FABER, B. J. 2015 TEM turbulence optimisation in stellarators. *Plasma Phys. Control. Fusion* **58** (1), 014006.

PUESCHEL, M. J., DANNERT, T. & JENKO, F. 2010 On the role of numerical dissipation in gyrokinetic Vlasov simulations of plasma microturbulence. *Comput. Phys. Commun.* **181** (8), 1428–1437.

PUESCHEL, M. J., FABER, B. J., CITRIN, J., HEGNA, C. C., TERRY, P. W. & HATCH, D. R. 2016 Stellarator turbulence: subdominant eigenmodes and quasilinear modeling. *Phys. Rev. Lett.* **116** (8), 085001.

PUESCHEL, M. J., GÖRLER, T., JENKO, F., HATCH, D. R. & CIANCIARA, A. J. 2013 On secondary and tertiary instability in electromagnetic plasma microturbulence. *Phys. Plasmas* **20** (10), 102308.

PUESCHEL, M. J., JENKO, F., TOLD, D. & BÜCHNER, J. 2011 Gyrokinetic simulations of magnetic reconnection. *Phys. Plasmas* **18** (11), 112102.

PUESCHEL, M. J., KAMMERER, M. & JENKO, F. 2008 Gyrokinetic turbulence simulations at high plasma beta. *Phys. Plasmas* **15** (10), 102310.

REWOLDT, G., KU, L.-P. & TANG, W. M. 2005 Comparison of microinstability properties for stellarator magnetic geometries. *Phys. Plasmas* **12** (10), 102512.

RUDAKOV, L. I. & SAGDEEV, R. Z. 1961 On the instability of a nonuniform rarefied plasma in a strong magnetic field. *Dokl. Akad. Nauk SSR* **138** (3), 581–583.

TALMADGE, J. N., ANDERSON, F. S. B., ANDERSON, D. T., DENG, C., GUTTENFELDER, W., LIKIN, K. M., LORE, J., SCHMITT, J. C. & ZHAI, K. 2008 Experimental tests of quasisymmetry in HSX. *Plasma Fusion Res.* **3**, S1002.

TERRY, P. W., BAVER, D. A. & GUPTA, S. 2006 Role of stable eigenmodes in saturated local plasma turbulence. *Phys. Plasmas* **13** (2), 022307.

TERRY, P. W., FABER, B. J., HEGNA, C. C., MIRNOV, V. V., PUESCHEL, M. J. & WHELAN, G. G. 2018 Saturation scalings of toroidal ion temperature gradient turbulence. *Phys. Plasmas* **25** (1), 012308.

TODA, S., NAKATA, M., NUNAMI, M., ISHIZAWA, A., WATANABE, T.-H. & SUGAMA, H. 2019 Transport simulation for helical plasmas by use of gyrokinetic transport model. *Plasma Fusion Res.* **14** (1), 3403061.

WEIR, G. M. 2014 Heat transport experiments on the HSX stellarator. PhD Thesis.

XANTHOPOULOS, P., COOPER, W. A., JENKO, F., TURKIN, Y., RUNOV, A. & GEIGER, J. 2009 A geometry interface for gyrokinetic microturbulence investigations in toroidal configurations. *Phys. Plasmas* **16** (8), 082303.

XANTHOPOULOS, P. & JENKO, F. 2007 Gyrokinetic analysis of linear microinstabilities for the stellarator Wendelstein 7-X. *Phys. Plasmas* **14** (4), 042501.

XANTHOPOULOS, P., MYNICK, H. E., HELANDER, P., TURKIN, Y., PLUNK, G. G., JENKO, F., GÖRLER, T., TOLD, D., BIRD, T. & PROLL, J. H. E. 2014 Controlling turbulence in present and future stellarators. *Phys. Rev. Lett.* **113** (15), 155011.

https://doi.org/10.1017/S0022377819000588 Published online by Cambridge University Press